APS/123-QED

Simulating Exciton Transport with Complex Absorbing Potentials

Dimitri Bazile,[1] Justin Caram,[1] Chern Chuang,[2] and Daniel Neuhauser[1,*]

[1]*Department of Chemistry and Biochemistry,*
University of California, Los Angeles, Los Angeles, CA 90095, USA

[2]*Department of Chemistry and Biochemistry,*
University of Nevada, Las Vegas, NV 89154, USA

(Dated: May 19, 2026)

Abstract

We introduce a stochastic framework based on complex absorbing potentials (CAPs) to investigate exciton transport in large molecular aggregates. Within this approach, CAPs act as non-Hermitian reservoirs and sinks that enable effective measurement of transport efficiency. We apply this framework to cyanine dye aggregates and examine how vacancy defects and system size influence exciton dynamics in two-dimensional sheets and quasi-one-dimensional tubes. We also introduce a CAPs-based classification scheme that links molecular packing in 2D aggregates to transport behavior. Our results demonstrate how aggregate topology and structural disorder govern exciton dynamics and provide guidance for designing materials with enhanced energy transport.

I. INTRODUCTION

Excitonic molecular aggregates are noncovalent assemblies of chromophores in which electronic excitations (excitons) are delocalized over multiple monomers, giving rise to photophysical properties distinct from those of isolated molecules [1]. In these systems, exciton transport arises from the interplay between coherent, wave-like propagation and incoherent hopping. This balance is strongly influenced by molecular organization, structural disorder, and packing [2–5]. Understanding how these factors govern exciton transport under realistic conditions is essential for improving optoelectronic materials, including organic light-emitting diodes, photovoltaic devices, and artificial photosynthetic systems. [6–8].

The relative arrangement of transition dipoles determines the sign and magnitude of intermolecular couplings, giving rise to the well-known distinction between J-aggregates (head-to-tail alignment) and H-aggregates (cofacial alignment) [9]. These aggregates are typically identified by red- and blue-shifted optical spectra relative to the monomer [10, 11]. More recent studies of two-dimensional (2D) and tubular cyanine dye aggregates have revealed excitonic behaviors that extend beyond this traditional classification, including I-aggregates, whose bright state is red-shifted while the band-edge structure resembles that of H-aggregates [12].

These findings highlight the importance of aggregate topology and dimensionality in

---

[*] dxn@ucla.edu

determining excitonic band structure and transport properties. Although both theoretical and experimental studies suggest that exciton transport is generally more efficient in J-aggregates than in H-aggregates [13, 14], spectral classification alone does not fully capture differences in transport behavior. This limitation motivates the development of transport-based classification schemes.

Energetic and structural disorder can localize excitons, a phenomenon known as Anderson localization which limits coherent transport [15, 16]. Energetic disorder arises from random variations in monomer excitation energies within an aggregate. This disorder can be spatially and temporally correlated or uncorrelated. Correlated disorder typically disrupts exciton transport less severely than uncorrelated disorder [17, 18]. These types of disorder have been widely investigated in molecular aggregates and related materials. [19–21].

Structural disorder can arise in several forms, including spatial variations in the relative positions and orientations of lattice sites, as well as the loss of coupling at a small number of sites due to defects [22, 23]. We refer to the latter as vacancy disorder. Vacancy effects have been investigated both theoretically and experimentally in systems such as light-harvesting nanotubes through the analysis of spectral changes induced by transient photodamage. [24]. However, a comprehensive understanding of how vacancy disorder affects transport efficiency across different aggregate geometries remains unexplored.

To systematically quantify how vacancy defects and system size influence exciton transport, and to distinguish transport behavior between H- and J-aggregates, theoretical frameworks that explicitly model transport efficiency are required. In the absence of environmental coupling, exciton dynamics reduces to a unitary evolution governed by the Hamiltonian of the system [25]. For weak system–bath coupling, the dynamics are described using Redfield theory [26] or Lindblad master equations [17, 27]. However, these approaches typically exhibit high computational scaling due to the matrix operations required for time propagation, although efficient approaches have been recently developed to address these limitations [28, 29].

In this work, we use complex absorbing potentials (CAPs) combined with stochastic methods to model exciton transport in molecular aggregates, enabling efficient simulations of exciton dynamics in large systems. CAPs are widely used to study metastable states with finite lifetimes, such as anions [30, 31], to facilitate wavepacket dynamics simulations [32, 33], and to model electron transport in mesoscopic conduction systems [34–36]. In electronic transport, CAPs can act as effective leads, allowing electrons to flow between channels and enabling the determination of transport properties in semiconductor systems [37]. More recently, CAPs have been applied to quantify exciton transport efficiency and loss rates in open quantum systems, including molecular aggregates and lossy cavity exciton transport models [38].

In molecular aggregates, CAPs act as exciton reservoirs and sinks that collect excitons, enabling direct tracking of exciton generation, propagation, and loss. To efficiently simulate large aggregates, we employ stochastic techniques. In particular, Chebyshev expansion to approximate the action of the Green's function [39] and stochastic trace methods are used to extract observables from the CAP formalism. These approaches circumvent full Hamiltonian operations and have been successfully applied to compute absorption spectra and density of states (DOS) in molecular aggregate systems [40, 41].

The paper is organized as follows. First, we introduce the CAP model within the Frenkel exciton framework for two-dimensional sheets and pseudo-one-dimensional tubular systems, including both one-dimensional and angle-dependent two-dimensional CAPs developed in this work. Next, we describe the stochastic methods used to compute transport metrics. In the Results section, we demonstrate that CAP-based transmission reproduces exciton delocalization trends under disorder. We then examine the effects of system size and vacancy defects in 2D sheets and tubular aggregates of TDBC and C8S3. Finally, we investigate the H–J regimes of TDBC and Cy7-DPA aggregates using angle-dependent CAPs and propose a new aggregate classification scheme. We conclude by highlighting directions for future research.

II. THEORETICAL METHODS

A. Frenkel Exciton Model, Vacancy and Disorder Effects

To model molecular aggregates with sheet and tubular structures, we employed the Frenkel exciton Hamiltonian

$$H_0 = \sum_n \epsilon_n |n\rangle\langle n| + \sum_{nm} J(n,m)|n\rangle\langle m|. \tag{1}$$

Here J represents the coupling between monomers n and m, and ϵ_n denotes the on site-energy plus the energetic disorder at monomer n. The coupling J is calculated using the extended dipole model,

$$J(n,m) = \frac{1}{4D}\frac{\mu^2}{d^2}\left(\frac{1}{r_{m+n+}} - \frac{1}{r_{m+n-}} - \frac{1}{r_{m-n+}} + \frac{1}{r_{m-n-}}\right). \tag{2}$$

μ is the effective dipole strength, d is the charge separation distance, D is the dielectric constant, and r_{nm} is the distance between monomers n and m. The ± subscripts denote the positions of the extended charges within each brick segment. Figure 1 illustrates these parameters for two brick monomers.

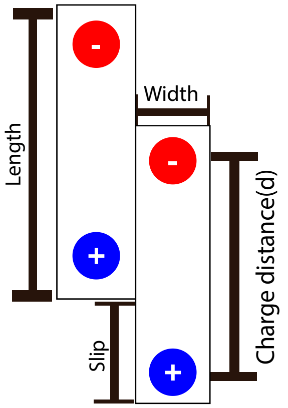

FIG. 1. Schematic representation of two brick-layer monomers showing the geometric parameters and extended charge distributions used to compute intermolecular coupling.

To introduce vacancies, we modify the Hamiltonian by removing contributions from monomers at vacant sites,

$$H = PH_0P. \tag{3}$$

Here P is a diagonal matrix of size $N_g \times N_g$, where N_g is the total number of monomer sites. Each diagonal element P_{ii} equals 1 if site i is occupied and 0 if it contains a vacancy; all off-diagonal elements are zero. The projected Hamiltonian H therefore removes all couplings to and from vacant sites. In the absence of vacancies, P reduces to the identity matrix and Eq.(3) recovers Eq. (1).

B. Complex Absorbing Potentials

Complex absorbing potentials (CAPs) are imaginary potentials added at the boundaries of a quantum system to simulate open boundary conditions. In transport calculations, CAPs mimic external leads by absorbing outgoing probability current and preventing artificial reflections at system boundaries [37, 42, 43]. This enables current injection at one boundary and absorption at the other. This approach is closely related to exciton transport models based on the Lindblad formalism, where one set of operators describes pumping into the excitonic manifold and another represents irreversible transfer to a sink. For example, Morales-Curiel and León-Montiel [44] studied transport efficiency in a two-dimensional J-aggregate by introducing a Lindblad sink operator and defining efficiency as the asymptotic population transferred to the sink.

C. 1D CAPs for Tubes and Sheets

For two-dimensional sheet aggregates, the number of transport channels depends on the system dimensions along the x and y directions. The x is along the brick width and the y direction is along the brick length. The transport along x involves n_y channels (the number of monomers along y), while the transport along y involves n_x channels. Pseudo-one-dimensional tubes can be viewed as sheets rolled along the x direction. In this geometry, CAPs extend along the tube height (z direction) and around the circumference (rotational direction). The number of channels is n_{rot} along the rotational direction and n_z along z. The CAP potentials are chosen as half-parabolas:

$$\hat{V}_I = \hat{V}_{IR} + \hat{V}_{IL} \tag{4}$$

$$\hat{V}_{IR} = \sum_n |n\rangle V_{IR}(w_n) \langle n| \tag{5}$$

$$\hat{V}_{IL} = \sum_n |n\rangle V_{IL}(w_n) \langle n| \tag{6}$$

$$V_{IL}(w_n) = \begin{cases} V_{0I} \dfrac{\left(w_{\min} + d_w - w_n\right)^2}{d_w^2}, & w_{\min} \leq w_n \leq w_{\min} + d_w, \\ 0, & \text{otherwise} \end{cases} \tag{7}$$

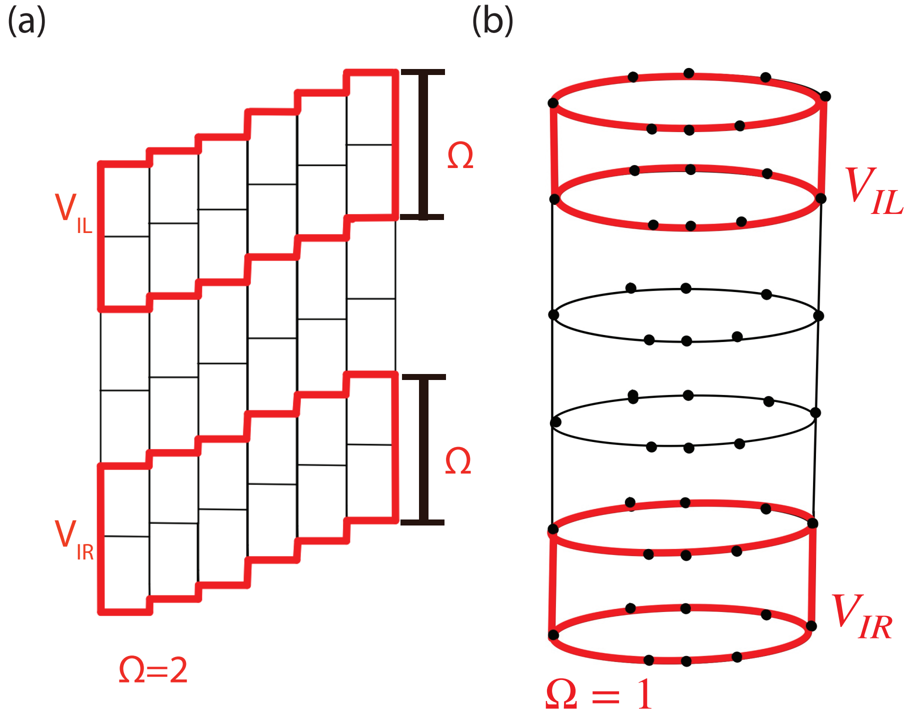

FIG. 2. Schematic representation of the complex absorbing potentials (CAPs) implemented in the model systems. (a) Two-dimensional aggregate sheet with $n_x = 6$ and $n_y = 6$. CAPs are applied along the brick width (x direction) and the probability current flows along the brick length(y-direction). The monomer unit length along the y-direction $\Omega = 2$. (b) Pseudo-one-dimensional tubular aggregate with $n_{\mathrm{rot}} = 8$ and $n_z = 6$. Black dots denote monomer centers. CAPs are applied along the rotational axis and the probability current travels along the tube height (z direction). The monomer unit along the z-direction for CAPs $\Omega = 1$.

$$V_{IR}(w_n) = \begin{cases} V_{0I}\,\dfrac{\left(w_n - (w_{\max} - d_w)\right)^2}{d_w^2}, & w_{\max} - d_w \leq w_n \leq w_{\max}, \\ 0, & \text{otherwise} \end{cases} \tag{8}$$

$\hat{V}_I$ represents the combined left and right potentials and V_{OI} denotes the maximum height of these potentials. The chosen coordinates, w_n, are based on the direction of the lattice vectors.

For 2D sheet at monomer n:

$$\mathbf{r}_n = \begin{bmatrix} x_n \\ y_n \end{bmatrix} = \begin{bmatrix} (n_2 - 1)W \\ (n_1 - 1)L + (n_2 - 1)S \end{bmatrix} \tag{9}$$

n_1 is the unit coordinate along the *length* (L) of the brick and n_2 is the unit coordinate along the *width* (W) and *slip* (S) is the offset between adjacent monomers in neighboring rows.

While for 1D tubes:

$$\mathbf{r}_n = \begin{bmatrix} x \\ y \\ z \end{bmatrix} = \begin{bmatrix} R\cos(n_2\phi_2 + n_1\gamma) \\ R\sin(n_2\phi_2 + n_1\gamma) \\ n_1 H \end{bmatrix} \tag{10}$$

$$\phi_2 = \frac{2\pi}{n_{rot}}(n_2 - 1) \tag{11}$$

R is the radius of each circular layer, γ is the twist angle between adjacent layers, and H is the vertical spacing between layers. The indices n_1 and n_2 denote the lattice coordinates along the tube circumference and height, respectively. Additional details on these parameters are given in Ref. [45].

For sheet geometries the CAPs are applied along the brick width (x direction) and transport along the y direction, such that $w_n = y_n$. This choice ensures that both the number of transport channels and the spacing between absorbing potentials remain constant even in the presence of *slip*. For tubular aggregates, the CAPs are applied along the tube rotational axis and transport along the tube height(z direction) such that,$w_n = z_n$. Channels in the rotational direction typically have low dimensionality (2–10), which makes CAP implementation along that direction impractical. A schematic of what this looks like for these geometries is shown in Fig 2.

The coordinates w_{min} and w_{max} denote the minimum and maximum positions along the chosen transport direction. The parameter d_w defines the length of the left and right absorbing regions. In the y direction, y_{min,n_2} and y_{max,n_2} correspond to the minimum and maximum coordinates of the n_2^{th} channel along x. This definition ensures that d_y remains constant across all channels:

$$y_{\text{min},n_2} = \mathrm{S} \cdot (n_2 - 1), \tag{12}$$

$$y_{\text{max},n_2} = \mathrm{L} \cdot (n_y - 1) + \text{slip} \cdot (n_2 - 1), \tag{13}$$

$$d_y = L \cdot (\Omega - 1), \tag{14}$$

$$z_{\text{min}} = 0, \tag{15}$$

$$z_{\text{max}} = \mathrm{H} \cdot (n_z - 1), \tag{16}$$

$$d_z = \mathrm{H} \cdot (\Omega - 1). \tag{17}$$

Ω is the unit length of the monomer of the left and right potentials. A visual representation of CAPs on molecular aggregate systems for sheets and tubes is shown in Fig. 2(a).

The energy-dependent transmission probability [34, 46] is

$$T(E) = 4\,\mathrm{Tr}\left[\frac{1}{E - H + iV_I}\,V_R\,\frac{1}{E - H - iV_I}\,V_L\right] = 4\,\mathrm{Tr}\left[G(E)\,V_R\,G^{\dagger}(E)\,V_L\right], \tag{18}$$

where $G(E)$ is the Green's function. To characterize transport, we define the thermally averaged transmission

$$\bar{T} = \frac{1}{Z}\sum_{i}^{n_g} T(\epsilon_i)\,e^{-\beta\epsilon_i} = \frac{1}{Z}\int\sum_i \delta(\epsilon_i - E)\,e^{-\beta E}\,T(E)\,dE = \frac{1}{Z}\int \rho(E)\,e^{-\beta E}\,T(E)\,dE, \tag{19}$$

with partition function

$$Z = \sum_i e^{-\beta\epsilon_i} = \int \rho(E)\,e^{-\beta E}\,dE, \tag{20}$$

where β is the inverse temperature and $\rho(E)$ is the density of states. The quantity $\bar{T}$ measures the overall transmission of the aggregate.

D. Angle-Dependent 2D CAP Potential

To model two-dimensional exciton transport, we construct angle-dependent CAPs from the lattice coordinates of each molecular brick. The procedure is:

1. Store the lattice coordinates and center them in the x–y plane

$$A(x_n, y_n) \rightarrow B = A - A_{\text{mid}}.$$

2. Convert the centered coordinates to cylindrical coordinates

$$B \to C(R, \theta), \qquad R = \sqrt{x_n^2 + y_n^2}, \qquad \theta_n = \arctan\left(\frac{y_n}{x_n}\right).$$

3. Select lattice points lying on a circle of radius R_a within a specified tolerance.

4. Construct the CAPs on the upper and lower arcs of the resulting circle of radius R_a.

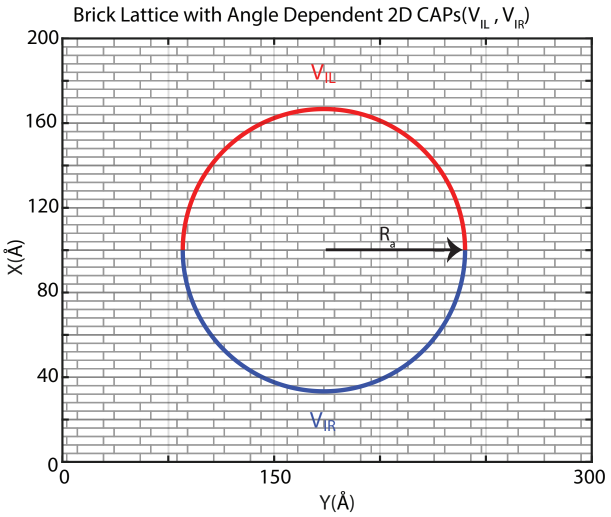

FIG. 3. Schematic of the 2D circular absorbing potentials applied to a 2D sheet geometry. The circular boundary defines the absorbing region of radius R_a.

The angle-dependent CAP potentials are defined as

$$V_{IL}(\theta_n, \theta_0) = \begin{cases} V_{0I}\,\sin^2(\theta_n - \theta_0), & 0 \le \theta_n < \pi, \\ 0, & \text{otherwise} \end{cases} \tag{21}$$

$$V_{IR}(\theta_n, \theta_0) = \begin{cases} V_{0I}\,\sin^2(\theta_n - \theta_0), & \pi \le \theta_n < 2\pi, \\ 0, & \text{otherwise} \end{cases} \tag{22}$$

Here θ_0 is a shift angle that controls coherent transport in the system. A schematic of the CAPs is shown in Fig. 3. With θ_0, we can tune which Bloch states contribute to the transmission.

E. Reducing Computational Cost

Experimentally relevant aggregates can extend hundreds of nanometers, and their properties converge only for sufficiently large systems. Conventional transmission calculations scale as $\mathcal{O}(N^3)$ due to matrix inversion and multiplication. To reduce this cost, we employ stochastic sampling with Chebyshev polynomial expansion to evaluate the Green's function [34, 36, 39]. The Hamiltonian is applied efficiently using 2D convolution, as previously demonstrated for molecular aggregates [40, 41]. This approach reduces the computational scaling from $\mathcal{O}(N^3)$ to $\mathcal{O}(N \log N)$.

The transmission probability can be written as

$$T(E) = 4 \, \mathrm{Tr}\big[A^\dagger(E) A(E)\big] \, , \tag{23}$$

$$A(E) = \hat{V}_R^{1/2} G(E) \hat{V}_L^{1/2}. \tag{24}$$

Using stochastic trace evaluation and Chebyshev expansion, $T(E)$ becomes

$$T(E) \approx \frac{4}{N_{\mathrm{stoc}}} \sum_{i=1}^{N_{\mathrm{stoc}}} \langle \chi_i | A'^\dagger A' | \chi_i \rangle, \tag{25}$$

$$A'(E) = \hat{V}_R^{1/2} \left(\sum_{n=0}^{N_{\mathrm{chb}}} a_n(E) \, \hat{Q}_n(\hat{H}', \hat{V}_I) \right) \hat{V}_L^{1/2}. \tag{26}$$

The stochastic vectors χ_i have elements randomly chosen as ± 1. The matrices $\hat{V}_R^{1/2}$ and $\hat{V}_L^{1/2}$ are the square roots of the diagonal elements of $\hat{V}_R$ and $\hat{V}_L$. The coefficients $a_n(E)$ are the Chebyshev expansion coefficients, and $\hat{Q}_n(\hat{H}, \hat{V}_I)$ are the associated Chebyshev polynomials.

The operator

$$\sum_{n=0}^{N_{\mathrm{chb}}} a_n(E) \hat{Q}_n(\hat{H}', \hat{V}_I)$$

represents the action of the Green's function on an arbitrary vector. The coefficients are

$$a_n = \frac{i(2 - \delta_{n,0})}{\Delta H \sin\phi} e^{-in\phi}, \tag{27}$$

$$\phi = \arccos\left(\frac{E - \bar{h}}{\Delta H} \right).$$

Here $\bar{h}$ and ΔH scale the Hamiltonian so that the eigenvalues of H' lie in $[-1, 1]$,

$$\bar{h} = \frac{\epsilon_{\text{max}} + \epsilon_{\text{min}}}{2}, \tag{28}$$

$$\Delta H = \frac{\epsilon_{\text{max}} - \epsilon_{\text{min}}}{2}, \tag{29}$$

$$H' = \frac{H - \bar{h}}{\Delta H}. \tag{30}$$

The quantities ϵ_{max} and ϵ_{min} denote the any upper and lower bounds ,repetitively, of H. The Chebyshev recursion is given by

$$\chi_0^\gamma = \hat{Q}_0(\hat{H}, \hat{V}_I)\chi^{ext} = \chi^{ext}, \tag{31}$$

$$\chi_1^\gamma = \hat{Q}_1(\hat{H}, \hat{V}_I)\chi^{ext} = e^{-\gamma}\hat{H}'\chi^{ext} \quad \gamma = \frac{\hat{V}_I}{\Delta H}. \tag{32}$$

and for $n > 1$,

$$\chi_n^\gamma = e^{-\gamma}\left(2\hat{H}'\chi_{n-1}^\gamma - e^{-\gamma}\chi_{n-2}^\gamma\right). \tag{33}$$

III. RESULTS/DISCUSSION

A. Simulation Specifications for CAPs

The parameters for the angle-dependent CAPs and the one-dimensional (1D) CAPs are listed in Tables I and II.

V_{OI} (cm^{-1})	Ω (Monomer Units)	N_{stoc}	N_{chb}	Temperature (K)
2130	$\frac{n_z}{4}$ (tubes), $\frac{n_y}{4}$ (sheets)	60	2000	300

TABLE I. Parameters used for the 1D CAP simulations in tube and sheet geometries.

V_{OI} (cm^{-1})	Radius of CAP (monomer units)	N_{stoc}	N_{chb}	Temperature (K)
2130	20	1200	2000	300

TABLE II. Parameters used for the 2D angle-dependent CAP simulations in sheet aggregates.

B. Predicting Delocalization Behavior with CAPs

Before using CAPs to measure exciton transport, we first tested whether they reproduce the delocalization behavior of known disorder effects. To do so, we compare the average transmission and the participation ratio (PR) in the presence of energetic disorder. PR quantifies exciton delocalization and is closely related to transport efficiency [25, 47].

Fig. 4 compares the PR with the average transmission computed using the 1D CAP potential as the energetic disorder strength (σ) increases. The transmission reproduces both the trend and overall shape of the PR. Thus, the average transmission predicts exciton delocalization and can serve as an alternative to PR/IPR(Inverse Participation ratio), with the additional advantage of providing directional information about transport.

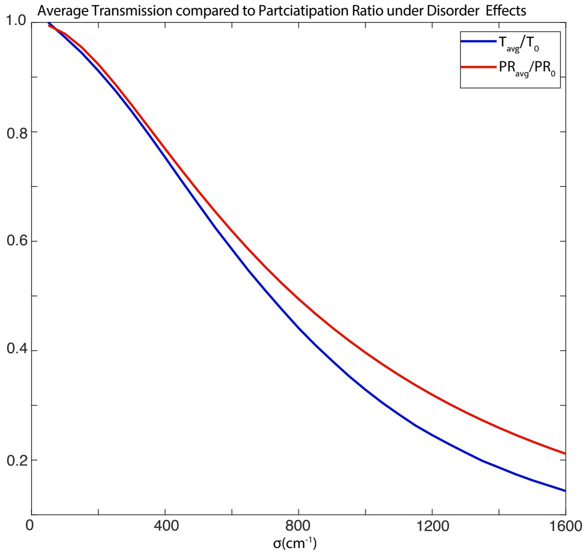

FIG. 4. Average participation ratio (PR_{avg}) and average transmission ($T_{\text{avg}} = \bar{T}$) as functions of disorder strength (σ). Both quantities are normalized to their respective values at zero disorder, $PR_0 = PR_{avg}(\sigma = 0)$ and $T_0 = T_{avg}(\sigma = 0)$. Results are shown for a 2D sheet system of size 20×100.

C. CAPs: Vacancy and Size Effects

We examine the effect of vacancy and system size on transmission. Fig 5 shows plots of the average transmission as a function of size and vacancy for both sheets and tubes, respectively. In both plots, the longer the path traversed by excitons in the presence of vacancies, the more the transmission decreases. This indicates that transmission is hindered more by the absolute number of sites removed than by the ratio of vacant sites to the number of monomers in the aggregate. The figure also shows that sheets are more resistant to vacancy effects than tubes. These results mirror the findings on diagonal disorder and dimensionality reported in [48], where 2D structures were shown from IPR calculations to be resistant to diagonal disorder than pseudo-1D tubes.

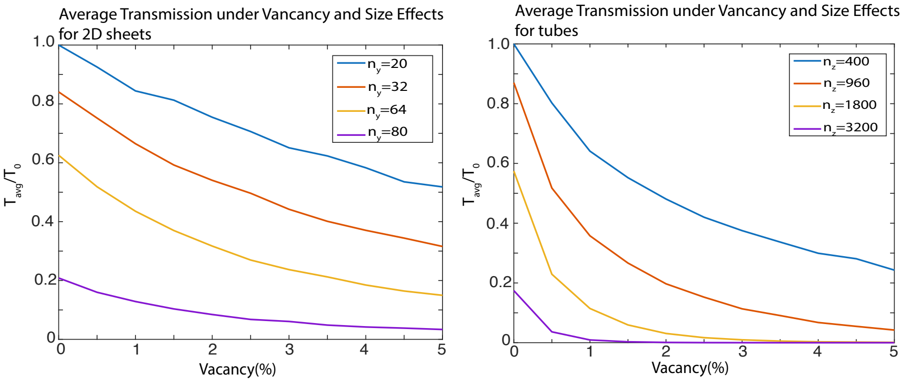

FIG. 5. (a) Plot of Average Transmission for 2D sheet aggregate with varying n_y and vacancy percentage. n_x is growing alongside n_x, keeping the ratio of $n_x : n_y$ at 5:1, meaning $n_x = 5n_y$ (b) Plot of Average Transmission for tubular aggregate with varying n_z and vacancy percentage. n_{rot} is constant at 5.

D. Transmission Calculations Using 2D CAPs

Next, we computed the angle-averaged transmission using the angle-dependent CAPs defined in Eqs. (21) and (22). The shift angle θ_0 and the slip parameter are varied across the H-, J-, and I-aggregate regimes for Cy7–DPA and TDBC. Screening this angle in different regimes allows us to see which bloch waves contribute the most to the transport. For each slip value, the transmission is averaged over all sampled angles according to Eq. (34).

$$\tilde{T} = \frac{1}{\pi} \int_0^{\pi} \bar{T}(\theta_0)\, d\theta_0. \tag{34}$$

This measure quantifies how the shift angle influences transport for a given slip, identifying regimes in which angular tuning either enhances, suppresses, or leaves the transmission largely unchanged. Fig. 6(a) shows $\tilde{T}$ for both aggregates as a function of slip. Two transmission regimes emerge: one with suppressed transmission and another with enhanced transmission. We denote these regimes as *I.S.-aggregates* (insulating-type aggregates) and

S-aggregates (semiconducting-type aggregates), respectively. The classification is aggregate-specific, and the corresponding slip ranges are listed in Table III.

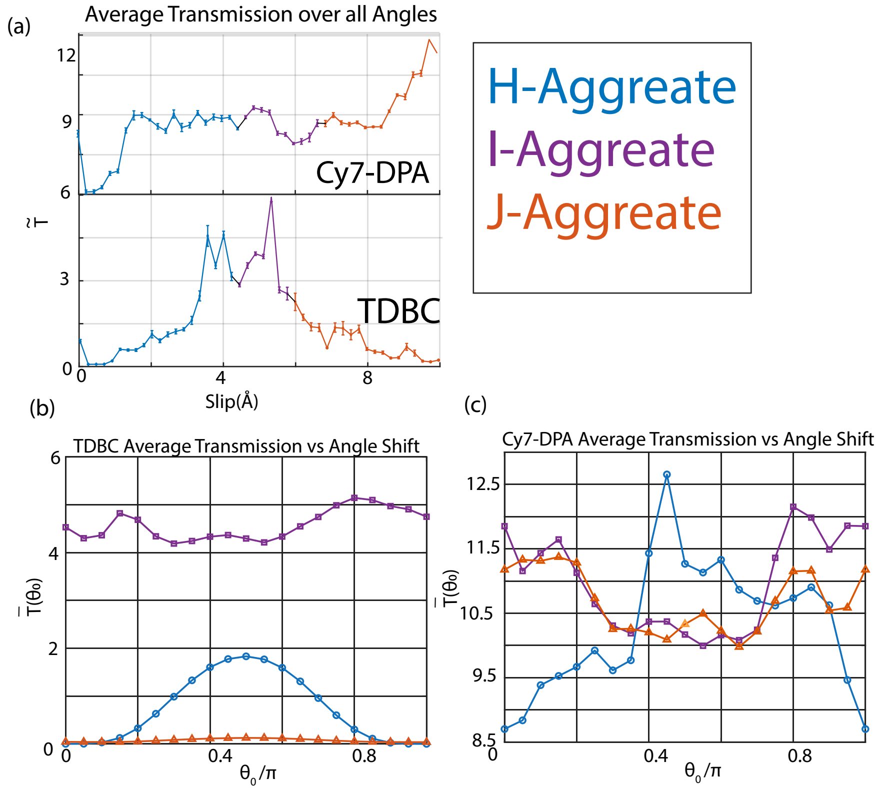

FIG. 6. Transmission calculated using angle-dependent CAPs with Aggregate Classification of H,J, I aggregate. (a) Angle-averaged transmission, $\tilde{T}$. (b) Average transmission as a function of shift angle, $\bar{T}(\theta_0)$, for TDBC. (c) Average transmission as a function of shift angle, $\bar{T}(\theta_0)$, for Cy7–DPA. Panels (b) and (c) show the angular dependence across different aggregate regimes (H-, I-, and J-aggregates), classified according to the slip parameter.

Aggregate	S-Aggregate Slip Regime (Å)	I.S.-Aggregate Slip Regime (Å)
Cy7-DPA	2.0–10	0.0–2.0
TDBC	3.6–4.4	0–3.6, 4.4–10

TABLE III. Slip parameter ranges defining the S- and I.S.-aggregate regimes for Cy7–DPA and TDBC.

The following classification between H, J, and I for TDBC and Cy7-DPA is based on the slip value for each aggregate, as referenced in [12]. For TDBC, the I-aggregate regime is entirely within the S-aggregate classification. For Cy7–DPA, all of the I- and J-aggregate regimes belong to the S-aggregate classification.

Fig. 6b and c show the averaged transmission dependent on the angle, $\bar{T}(\theta_0)$, for both TDBC and Cy7–DPA. The figure shows maximum transmission in the H-aggregate regime at $\theta_0 = \frac{\pi}{2}$. Moving away from this angle dramatically reduces the transmission, unlike in other aggregate types. In contrast, the I-aggregate regime exhibits the smallest variation in transmission across shift angles.

To rationalize the trends observed above, we analyze the contributions of individual k-states within the S- and I.S.-aggregate regimes as a function of θ_0. The contribution from each k-state to the transmission is quantified by

$$\bar{T}(k_x, k_y, \theta_0) = \frac{1}{Z} \int \rho(E)\, e^{-\beta E}\, T(k_x, k_y, E, \theta_0)\, dE, \tag{35}$$

$$T(k_x, k_y, E, \theta_0) = 4\, \langle k_x, k_y | A(E, \theta_0)\, A^{\dagger}(E, \theta_0) | k_x, k_y \rangle, \tag{36}$$

with the Bloch wave states $|k_x, k_y\rangle$ defined as

$$\langle j_x, j_y \mid k_x, k_y \rangle = \frac{1}{\sqrt{N}} \exp\!\left(i2\pi \frac{k_x j_x}{n_x} \right) \exp\!\left(i2\pi \frac{k_y j_y}{n_y} \right), \tag{37}$$

where $k_x = 0, 1, 2, \ldots, (n_x - 1)$ and $k_y = 0, 1, 2, \ldots, (n_y - 1)$.

Fig. 7 and 8 show the contributions of individual k-states calculated using Eq. (35). As illustrated in these figures, the control parameter θ_0 selects the subset of k-states that dominate the transmission. For the S-aggregate regime in both TDBC and Cy7–DPA, the transmission is maximized by states near $(k_x, k_y) = \left(\frac{n_x - 1}{2}, \frac{n_y - 1}{2}\right)$ when $\theta_0 = \pi/2$. In contrast, the dominant k-states in the I.S.-aggregate regime differ between the two systems. For TDBC, the largest contributions arise from states near $(k_x, k_y) = (0, n_y - 1)$ and $(n_x - 1, 0)$ when $\theta_0 = 0$ and π. For Cy7-DPA, the maximum transmission in the I.S.-aggregate regime also occurs near $(k_x, k_y) = \left(\frac{n_x - 1}{2}, \frac{n_y - 1}{2}\right)$ at $\theta_0 = \pi/2$, but with a substantially smaller number of contributing states compared to the S-aggregate regime. In general, transmission is maximized when contributing k-states are located near the center of the Brillouin zone and is further enhanced when $\theta_0 = \pi/2$.

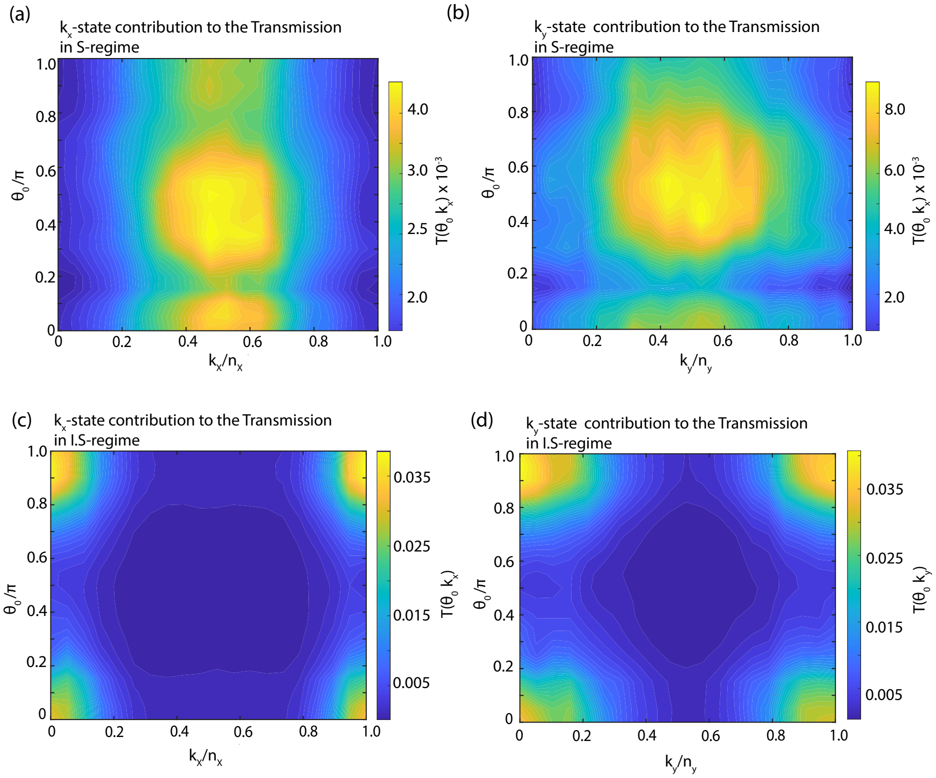

FIG. 7. k-state contribution of transmission for contour plots of TDBC under varying θ_0 in S and I.S regimes. Top: S-aggregate regime (slip = 4 Å). (a) k_x (b) k_y Bottom: I.S-aggregate regime (slip = 9 Å). (c) k_x (d) k_y In each case: For k_x contribution, $k_y = 0$, (b) For k_y contribution, $k_x = 0$.

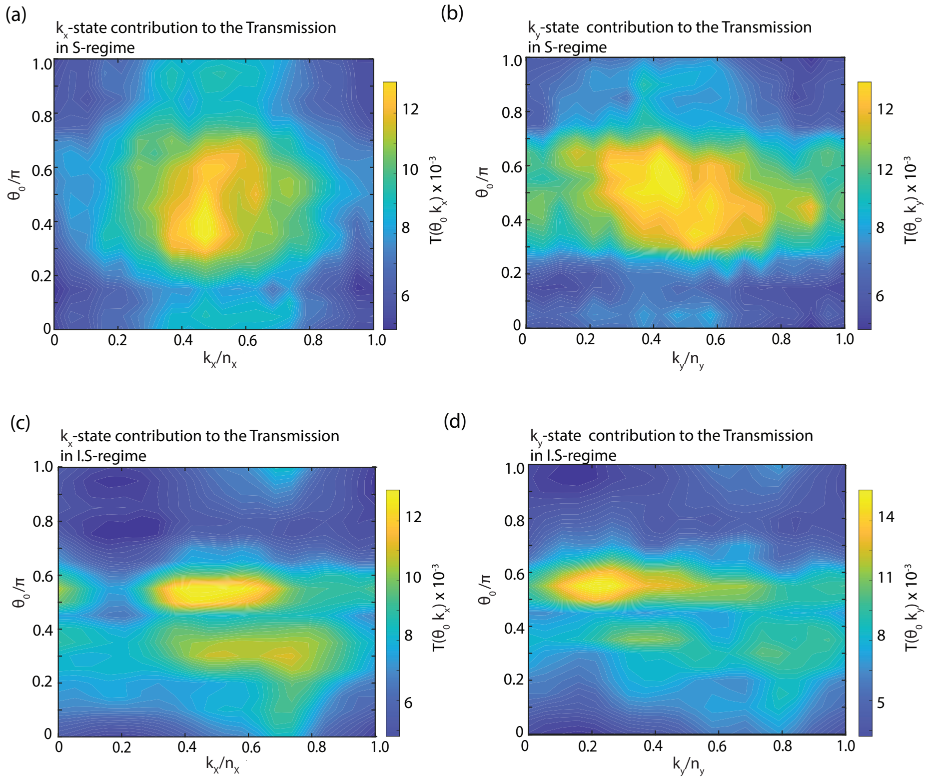

FIG. 8. k-state contribution of transmission for contour plots of Cy7-DPA under varying θ_0 in S and I.S regimes. Top: S-aggregate regime (slip = 4 Å). (a) k_x (b) k_y Bottom: I.S-aggregate regime (slip = 1 Å). (c) k_x (d) k_y In each case: For k_x contribution, $k_y = 0$, (b) For k_y contribution, $k_x = 0$.

IV. CONCLUSION

This work demonstrates the capability of complex absorbing potentials (CAPs) to probe exciton dynamics in molecular aggregate sheets and tubes, and to compare the spectral characteristics associated with different types of disorder. Stochastic methods enable the screening of larger systems, bringing the results closer to experimentally relevant length scales. Using these techniques, the effects of vacancies and energetic disorder on exciton transport in two-dimensional aggregate sheets are successfully modeled. The results indicate that reduced transmission correlates with diminished transport, allowing us to predict how vacancies and disorder impede exciton motion. We also identify two distinct aggregate regimes based on transmission behavior and, consequently, coherent transport properties. The angle-dependent CAP framework provides a systematic approach for linking molecular packing, aggregate classification, and transport efficiency in two-dimensional molecular aggregates.

In future work, these methods will be extended to additional systems and combined with complementary approaches, including cavity-coupled systems and biexcitonic systems. Using CAPs in time-evolution studies for molecular aggregates has the advantage of suppressing backscattering at boundaries, enabling more accurate predictions of time-dependent quantities such as the diffusion constant, localization length, and average travel time.

[1] Brixner, T.; Hildner, R.; Köhler, J.; Lambert, C.; Würthner, F. Exciton Transport in Molecular Aggregates – From Natural Antennas to Synthetic Chromophore Systems. *Advanced Energy Materials* **2017**, *7*.

[2] Barford, W.; Duffy, C. D. P. Role of quantum coherence and energetic disorder in exciton transport in polymer films. *Physical Review B* **2006**, *74*.

[3] Popp, W.; Brey, D.; Binder, R.; Burghardt, I. Quantum Dynamics of Exciton Transport and Dissociation in Multichromophoric Systems. *Annual Review of Physical Chemistry* **2021**, *72*, 591–616.

[4] Wong, C. Y.; Cotts, B. L.; Wu, H.; Ginsberg, N. S. Exciton dynamics reveal aggregates with intermolecular order at hidden interfaces in solution-cast organic semiconducting films. *Nature Communications* **2015**, *6*.

[5] Lebedenko, A. N.; Grynyov, R. S.; Guralchuk, G. Y.; Sorokin, A. V.; Yefimova, S. L.; Malyukin, Y. V. Coherent Mechanism of Exciton Transport in Disordered J-Aggregates. *The Journal of Physical Chemistry C* **2009**, *113*, 12883–12887.

[6] Kalinowski, J. *Electrical and Related Properties of Organic Solids*; Springer Netherlands, 1997; p 167–206.

[7] Hedley, G. J.; Ruseckas, A.; Samuel, I. D. W. Light Harvesting for Organic Photovoltaics. *Chemical Reviews* **2016**, *117*, 796–837.

[8] Saikin, S. K.; Eisfeld, A.; Valleau, S.; Aspuru-Guzik, A. Photonics meets excitonics: natural and artificial molecular aggregates. *Nanophotonics* **2013**, *2*, 21–38.

[9] Kasha, M. Energy Transfer Mechanisms and the Molecular Exciton Model for Molecular Aggregates. *Radiation Research* **1963**, *20*, 55.

[10] Jelley, E. E. Molecular, Nematic and Crystal States of I: I-Diethyl–Cyanine Chloride. *Nature* **1937**, *139*, 631–631.

[11] Jelley, E. E. Spectral Absorption and Fluorescence of Dyes in the Molecular State. *Nature* **1936**, *138*, 1009–1010.

[12] Deshmukh, A. P.; Geue, N.; Bradbury, N. C.; Atallah, T. L.; Chuang, C.; Pengshung, M.; Cao, J.; Sletten, E. M.; Neuhauser, D.; Caram, J. R. Bridging the gap between H- and J-aggregates: Classification and supramolecular tunability for excitonic band structures in two-dimensional molecular aggregates. *Chemical Physics Reviews* **2022**, *3*.

[13] Würthner, F.; Kaiser, T. E.; Saha-Möller, C. R. J-Aggregates: From Serendipitous Discovery to Supramolecular Engineering of Functional Dye Materials. *Angewandte Chemie International Edition* **2011**, *50*, 3376–3410.

[14] Petrenko, V.; Dimitriev, O.; Slominskii, Y.; Smirnova, A. Efficient energy transfer between J-aggregates of thiamonomethinecyanine dyes. *Chemical Physics Letters* **2015**, *621*, 22–28.

[15] Anderson, P. W. Absence of Diffusion in Certain Random Lattices. *Physical Review* **1958**, *109*, 1492–1505.

[16] Evensky, D. A.; Scalettar, R. T.; Wolynes, P. G. Localization and dephasing effects in a time-dependent Anderson Hamiltonian. *The Journal of Physical Chemistry* **1990**, *94*, 1149–1154.

[17] Uchiyama, C.; Munro, W. J.; Nemoto, K. Environmental engineering for quantum energy transport. *npj Quantum Information* **2018**, *4*.

[18] Lee, C. K.; Shi, L.; Willard, A. P. Modeling the Influence of Correlated Molecular Disorder

on the Dynamics of Excitons in Organic Molecular Semiconductors. *The Journal of Physical Chemistry C* **2018**, *123*, 306–314.

[19] Akselrod, G. M.; Deotare, P. B.; Thompson, N. J.; Lee, J.; Tisdale, W. A.; Baldo, M. A.; Menon, V. M.; Bulović, V. Visualization of exciton transport in ordered and disordered molecular solids. *Nature Communications* **2014**, *5*.

[20] Reineker, P.; Warns, C.; Neidlinger, T.; Barvík, I. Exciton transport in dynamically disordered molecular aggregates: influence on optical line shapes. *Chemical Physics* **1993**, *177*, 715–726.

[21] Pant, R.; Wüster, S. Excitation transport in molecular aggregates with thermal motion. *Physical Chemistry Chemical Physics* **2020**, *22*, 21169–21184.

[22] Domínguez-Adame, F.; Malyshev, V. Frenkel excitons in one-dimensional systems with correlated disorder. *Journal of Luminescence* **1999**, *83–84*, 61–67.

[23] Biroli, G.; Monasson, R. A single defect approximation for localized states on random lattices. *Journal of Physics A: Mathematical and General* **1999**, *32*, L255–L261.

[24] Doria, S.; Sinclair, T. S.; Klein, N. D.; Bennett, D. I. G.; Chuang, C.; Freyria, F. S.; Steiner, C. P.; Foggi, P.; Nelson, K. A.; Cao, J.; Aspuru-Guzik, A.; Lloyd, S.; Caram, J. R.; Bawendi, M. G. Photochemical Control of Exciton Superradiance in Light-Harvesting Nanotubes. *ACS Nano* **2018**, *12*, 4556–4564.

[25] Giannini, S.; Peng, W.-T.; Cupellini, L.; Padula, D.; Carof, A.; Blumberger, J. Exciton transport in molecular organic semiconductors boosted by transient quantum delocalization. *Nature Communications* **2022**, *13*.

[26] Ishizaki, A.; Fleming, G. R. On the adequacy of the Redfield equation and related approaches to the study of quantum dynamics in electronic energy transfer. *The Journal of Chemical Physics* **2009**, *130*.

[27] Mülken, O.; Schmid, T. Environment-assisted quantum transport and trapping in dimers. *Physical Review E* **2010**, *82*.

[28] Kondov, I.; Kleinekathöfer, U.; Schreiber, M. Stochastic unraveling of Redfield master equations and its application to electron transfer problems. *The Journal of Chemical Physics* **2003**, *119*, 6635–6646.

[29] Adhikari, S.; Baer, R. Stochastically Bundled Dissipators for the Quantum Master Equation. *Journal of Chemical Theory and Computation* **2025**, *21*, 4142–4150.

[30] Dempwolff, A. L.; Belogolova, A. M.; Sommerfeld, T.; Trofimov, A. B.; Dreuw, A. CAP/EA-

ADC method for metastable anions: Computational aspects and application to π^* resonances resonances of norbornadiene and 1, 4-cyclohexadiene. *The Journal of Chemical Physics* **2021**, *155*.

[31] Gyamfi, J. A.; Jagau, T.-C. Ab Initio Molecular Dynamics of Temporary Anions Using Complex Absorbing Potentials. *The Journal of Physical Chemistry Letters* **2022**, *13*, 8477–8483.

[32] Vibok, A.; Balint-Kurti, G. G. Parametrization of complex absorbing potentials for time-dependent quantum dynamics. *The Journal of Physical Chemistry* **1992**, *96*, 8712–8719.

[33] Neuhasuer, D.; Baer, M. The time-dependent Schrödinger equation: Application of absorbing boundary conditions. *The Journal of Chemical Physics* **1989**, *90*, 4351–4355.

[34] Collepardo-Guevara, R.; Walter, D.; Neuhauser, D.; Baer, R. A Hückel study of the effect of a molecular resonance cavity on the quantum conductance of an alkene wire. *Chemical Physics Letters* **2004**, *393*, 367–371.

[35] Landauer, R. Conductance determined by transmission: probes and quantised constriction resistance. *Journal of Physics: Condensed Matter* **1989**, *1*, 8099–8110.

[36] de Castro, S. G.; Ferreira, A.; Bahamon, D. A. Efficient Chebyshev polynomial approach to quantum conductance calculations: Application to twisted bilayer graphene. *Physical Review B* **2023**, *107*.

[37] Datta, S. *Electronic transport in Mesoscopic Systems*; Cambridge Univ. Press, 1999.

[38] Sharma, D.; Bose, A. Non-Hermitian State-to-State Analysis of Transport in Aggregates with Multiple Endpoints. *Journal of Chemical Theory and Computation* **2025**, *21*, 5858–5866.

[39] Mandelshtam, V. A.; Taylor, H. S. Spectral projection approach to the quantum scattering calculations. *The Journal of Chemical Physics* **1995**, *102*, 7390–7399.

[40] Bradbury, N. C.; Chuang, C.; Deshmukh, A. P.; Rabani, E.; Baer, R.; Caram, J. R.; Neuhauser, D. Stochastically Realized Observables for Excitonic Molecular Aggregates. *The Journal of Physical Chemistry A* **2020**, *124*, 10111–10120.

[41] Bradbury, N. C.; Ribeiro, R. F.; Caram, J. R.; Neuhauser, D. Stochastic methodology shows molecular interactions protect two-dimensional polaritons. *Physical Review B* **2024**, *109*.

[42] Varga, K. Quantum transport calculations using complex absorbing potentials. *physica status solidi (b)* **2009**, *246*, 1407–1412.

[43] Xie, H.; Kwok, Y.; Jiang, F.; Zheng, X.; Chen, G. Complex absorbing potential based Lorentzian fitting scheme and time dependent quantum transport. *The Journal of Chemi-*

cal Physics **2014**, *141*.

[44] Morales-Curiel, L. F.; León-Montiel, R. d. J. Photochemical dynamics under incoherent illumination: Light harvesting in self-assembled molecular J-aggregates. *The Journal of Chemical Physics* **2020**, *152*.

[45] Didraga, C.; Klugkist, J. A.; Knoester, J. Optical Properties of Helical Cylindrical Molecular Aggregates: The Homogeneous Limit. *The Journal of Physical Chemistry B* **2002**, *106*, 11474–11486.

[46] Seideman, T.; Miller, W. H. Calculation of the cumulative reaction probability via a discrete variable representation with absorbing boundary conditions. *The Journal of Chemical Physics* **1992**, *96*, 4412–4422.

[47] Sneyd, A. J. et al. Efficient energy transport in an organic semiconductor mediated by transient exciton delocalization. *Science Advances* **2021**, *7*.

[48] Chuang, C.; Lee, C. K.; Moix, J. M.; Knoester, J.; Cao, J. Quantum Diffusion on Molecular Tubes: Universal Scaling of the 1D to 2D Transition. *Physical Review Letters* **2016**, *116*.